

Topological axion states in magnetic insulator MnBi_2Te_4 with the quantized magnetoelectric effect

Dongqin Zhang,¹ Minji Shi,¹ Tongshuai Zhu,¹ Dingyu Xing,^{1,2} Haijun Zhang,^{1,2,*} and Jing Wang^{3,2,4,†}

¹*National Laboratory of Solid State Microstructures,
School of Physics, Nanjing University, Nanjing 210093, China*

²*Collaborative Innovation Center of Advanced Microstructures, Nanjing University, Nanjing 210093, China*

³*State Key Laboratory of Surface Physics, Department of Physics, Fudan University, Shanghai 200433, China*

⁴*Institute for Nanoelectronic Devices and Quantum Computing, Fudan University, Shanghai 200433, China*

(Dated: August 25, 2022)

Topological states of quantum matter have attracted great attention in condensed matter physics and materials science. The study of time-reversal-invariant topological states in quantum materials has made tremendous progress. However, the study of magnetic topological states falls much behind due to the complex magnetic structures. Here, we predict the tetradymite-type compound MnBi_2Te_4 and its related materials host topologically nontrivial magnetic states. The magnetic ground state of MnBi_2Te_4 is an antiferromagnetic topological insulator state with a large topologically non-trivial energy gap (~ 0.2 eV). It is the parent state for the axion state, which has gapped bulk and surface states, and the quantized topological magnetoelectric effect. The ferromagnetic phase of MnBi_2Te_4 might lead to a minimal ideal Weyl semimetal which has never been discovered in real materials. We further present a simple and unified continuum model to capture the salient topological features of this kind of materials.

The recent discovery of the time-reversal-invariant (TRI) topological insulator [1–4] brings the opportunity to realize a large family of exotic topological phenomena through magnetically gapping the topological gapless surface states [5–36]. Tremendous efforts have been made to introduce magnetism into TRI topological insulators. Most successful example is the first realization of the quantum anomalous Hall (QAH) effect in Cr-doped $(\text{Bi,Sb})_2\text{Te}_3$ topological insulator thin films [28, 37, 38]. Aside from the dilute magnetic topological insulators, intrinsic magnetic materials expect to provide a clean platform to study magnetic topological states with new interesting topological phenomena. Some magnetic topological states have been theoretically proposed [39], such as antiferromagnetic topological insulator [29], dynamical axion field [40], magnetic Dirac semimetal [32, 33, 41, 42], and magnetic Weyl semimetals [30, 31, 43]. Unfortunately, none of them have been realized in experiments. Therefore, realistic magnetic topological materials are highly desired. The class of MnBi_2Te_4 materials predicted in this Letter provide an ideal platform for emergent magnetic topological phenomena, such as, the antiferromagnetic topological insulator, the topological axion state with quantized topological magnetoelectric effect, the minimal ideal Weyl semimetal, the QAH effect, two-dimensional ferromagnetism and so on.

Electronic structure. The tetradymite-type compounds XA_2B_4 , also written as $\text{XB}\cdot\text{A}_2\text{B}_3$ with $\text{X} = \text{Ge}, \text{Sn}, \text{Pb}$ or Mn , $\text{A} = \text{Sb}$ or Bi , and $\text{B} = \text{Se}$ or Te , crystallize in a rhombohedral crystal structure with the space group D_{3d}^5 (No. 166) with seven atoms in one unit cell. We take MnBi_2Te_4 as an example, which has been successfully synthesized in experiments [44]. It has layered structures with a triangle lattice, shown in Fig. 1. The

trigonal axis (three-fold rotation symmetry) is defined as the z axis, a binary axis (two-fold rotation symmetry) is defined as the x axis and a bisectrix axis (in the reflection plane) is defined as the y axis for the coordinate system. The material consists of seven-atom layers (e.g. $\text{Te1-Bi1-Te2-Mn-Te3-Bi2-Te4}$) arranged along the z direction, known as a septuple layer, which could also be simply viewed as the intergrowth of (111) plane of rock-salt structure MnTe within the quintuple layer of topological insulator Bi_2Te_3 (see Fig. 1a and c) [10]. The coupling between different septuple layers is the van der Waals type. The existence of inversion symmetry, with the Mn site as the inversion center, enables us to construct eigenstates with definite parity.

Based on first-principles calculations, we find that each Mn atom in MnBi_2Te_4 tends to lose two electrons and have half filled d orbitals. We performed total energy calculations for different magnetic phases for the three-dimensional MnBi_2Te_4 , and the results are listed in Fig. 1(e), showing that the A-type antiferromagnetic phase with the out-of-plane easy axis, denoted as AFM1 (seen in Fig. 1(a)), is the magnetic ground state. It is ferromagnetic within the xy plane in each septuple layer, and antiferromagnetic between neighbor septuple layers along the z direction, consisting with the previous report [45]. The total energy of the A-type antiferromagnetic phase AFM2 with the in-plane easy axis is slightly higher than that of AFM1, and much lower than that of ferromagnetic phase FM1 with the out-of-plane easy axis, which indicates that the magnetic anisotropy is weaker than the effective magnetic exchange interaction between Mn atoms in neighbor septuple layers. The ferromagnetic phase FM2 with in-plane easy axis has the highest energy. In the following discussion, we would focus on the AFM1

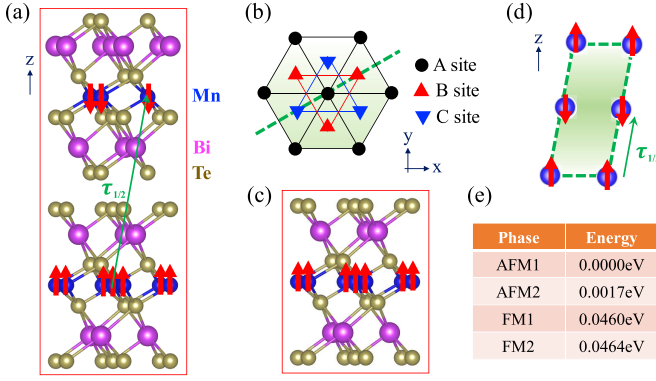


FIG. 1. Crystal structure and magnetic structure. (a), The unit cell of antiferromagnetic MnBi_2Te_4 consists of two septuple layers. The red arrows represent the spin moment of Mn atom. The green arrow denotes for the half translation operator $\tau_{1/2}$. (b), Schematic top view along the z -direction. The triangle lattice in one septuple layer has three different positions, denoted as A, B and C. The dotted green line is used for the (011) plane. (c), The unit cell of ferromagnetic MnBi_2Te_4 has one septuple layer. (d), The schematic of the (011) plane, with the blue balls denoting Mn atoms. (e), The total energy for different magnetic ordered states obtained from first-principles calculations.

(the magnetic ground state) and FM1 (possibly realized through an external magnetic field) states.

Firstly we investigate the magnetic ground state with the AFM1 order. The band structures of AFM1 state without and with spin-orbit coupling (SOC) are shown in Fig. 2(a) and 2(b), respectively. The time-reversal symmetry Θ is broken, however, a combined symmetry $\mathcal{S} = \Theta\tau_{1/2}$ is preserved, where $\tau_{1/2}$ is the half translation operator connecting nearest spin-up and -down Mn atomic layers, marked in Fig. 1(a). The antiunitary operator \mathcal{S} could also lead to a \mathcal{Z}_2 topological invariant [29], which is well defined on the Brillouin-zone plane with $\mathbf{k} \cdot \tau_{1/2} = 0$. One can see an anti-crossing feature around the Γ point from the band inversion, suggesting that MnBi_2Te_4 might be topologically nontrivial. Since the inversion symmetry \mathcal{I} is still preserved in this case, the parity is well defined at time-reversal-invariant momenta (TRIM) in the Brillouin zone, and the Fu and Kane method [46] can be employed to calculate the \mathcal{Z}_2 invariant. Here we only need consider the four TRIM (Γ and three F) with $\mathbf{G} \cdot \tau_{1/2} = n\pi$. As expected, by turning on SOC, the parity of one occupied band is changed at Γ point from the band inversion between the $|P1_z^+\rangle$ of Bi and the $|P2_z^-\rangle$ of Te, schematically shown in Fig. 2(d), whereas the parity remains unchanged for all occupied bands at the other three momenta F (see Fig. 2(e)), so the \mathcal{Z}_2 invariant is obtained to be 1. We also employ the Willson loop method [47] to confirm the \mathcal{Z}_2 invariant in Fig. 2(f), concluding that antiferromagnetic MnBi_2Te_4 is an antiferromagnetic topological insulator with $\mathcal{Z}_2 = 1$.

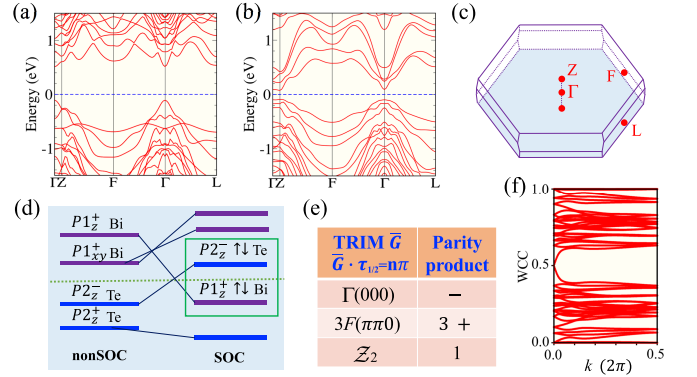


FIG. 2. Electronic structure of AFM1 MnBi_2Te_4 . (a),(b), The band structure of AFM1 state without (a) and with (b) SOC. (b), The bands are two-fold degenerate due to conserved \mathcal{I} and \mathcal{S} . (c), Brillouin zone of MnBi_2Te_4 . The four inequivalent TRIM are $\Gamma(0,0,0)$, $L(\pi,0,0)$, $F(\pi,\pi,0)$ and $Z(\pi,\pi,\pi)$. (d), Schematic diagram of the band inversion at the Γ point. The green dashed line represents the Fermi level. (e), The parity product at the TRIM (Γ and $3F$) with $\mathbf{G} \cdot \tau_{1/2} = n\pi$. The parity product is ‘-’ at Γ point, and the topological invariant \mathcal{Z}_2 is 1. (f), The Wannier charge centers (WCC) is calculated in the plane with Γ and $3F$, confirming $\mathcal{Z}_2 = 1$.

Especially, a large energy gap of about 0.2eV is obtained in Fig. 2(b).

The existence of topological surface states is one of the most important properties of the topological insulators. However, the topological insulator state in antiferromagnetic MnBi_2Te_4 protected by \mathcal{S} symmetry is topological in a weaker sense than the strong topological insulator protected by Θ symmetry, which manifests in that the existence of gapless surface state depends on the surface plane. As shown in Fig. 4(a) and 4(c), there is gapped surface states on the (111) surface accompanied by a triangular Fermi surface, for \mathcal{S} symmetry is broken. Only on the \mathcal{S} symmetry preserving surfaces such as (011) surface, the gapless surface states are topological protected. As shown in Fig. 4(b), topological surface state forms a single Dirac-cone-type dispersion at the Γ point on the (011) surface.

For the FM1 state of MnBi_2Te_4 , the band structures without and with the SOC effect are shown in Fig. 3. When the SOC effect is included, MnBi_2Te_4 is a ferromagnetic insulator with the experimental lattice constants (a_0, c_0), shown in Fig. 3(b). Interestingly, we find that the band structure is sensitive with the lattice constants. When we slightly extend the lattice constants, it first becomes a type-II Weyl semimetal with $(1.005a_0, 1.005c_0)$ and then becomes a minimal ideal Weyl semimetal with $(1.01a_0, 1.01c_0)$, hosting two Weyl points at the Fermi level without other bulk bands mixing, shown in Fig. 3(c)-(d). This is the first minimal ideal Weyl semimetal discovered in realistic materials. The Willson loop calculations, shown in Fig. 3(e) and

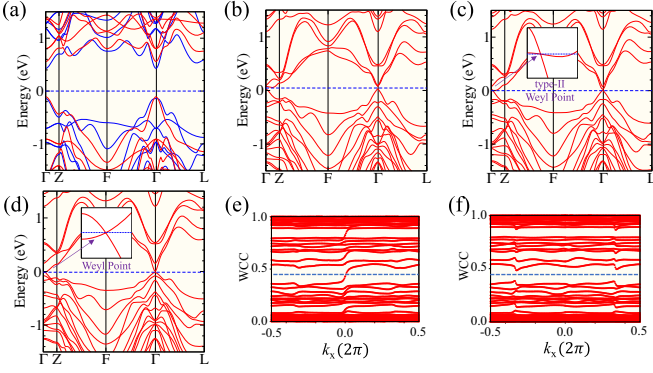


FIG. 3. Electronic structure of FM1 MnBi_2Te_4 . (a), Band structure for FM1 state without SOC. The dashed line indicates the Fermi level. The red/blue lines are spin-up/-down bands. (b)-(d), Band structures for FM1 state with SOC are calculated by the LDA+U ($U = 3$ eV) functional with experimental lattice constants (a_0, c_0) in (b), extended lattice constants ($1.005a_0, 1.005c_0$) in (c) and ($1.01a_0, 1.01c_0$) in (d), respectively. The system has the transition from ferromagnetic insulator to type-II Weyl semimetal, and finally to ideal Weyl semimetal. (e),(f), The evolution of WCC along the k_x direction in the $k_z = 0$ plane (e) and in the $k_z = \pi$ plane (f). The WCCs cross the reference horizontal line once in (e), indicating the Chern number $C = 1$ in the $k_z = 0$ plane. Oppositely, the WCCs don't cross the reference line in (f), indicating the Chern number $C = 0$ in the $k_z = \pi$ plane.

3(f), suggest that the Chern number $C = 1$ at the $k_z = 0$ plane, and $C = 0$ at the $k_z = \pi$ plane, which is consistent with the ideal Weyl semimetal band structure in Fig. 3(d). Furthermore, the surface states of FM1 state on different typical surfaces are calculated. In Fig. 4(d), bulk states projected on the (111) surface have no energy gap, for the two Weyl points are exactly projected to the surface $\bar{\Gamma}$ point. In Fig. 4(e) and 4(f), one can clearly see the surface Fermi arcs connecting to the two ideal Weyl points separated by ($\sim 0.06 \text{ \AA}^{-1}$).

Low-energy effective model. As the topological nature is determined by the physics near the Γ point, a simple effective Hamiltonian can be written down to characterize the low-energy long-wavelength properties of the system. We start from the four low-lying states $|P1_z^+, \uparrow(\downarrow)\rangle$ and $|P2_z^-, \uparrow(\downarrow)\rangle$ at the Γ point. Here the superscripts '+', '-' stand for the parity of the corresponding states. Without the SOC effect, around the Fermi energy, the bonding state $|P1_z^+\rangle$ of two Bi layers stays above of the antibonding state $|P2_z^-\rangle$ of two Te layers (Te1 and Te4 in septuple layers). As shown in Fig. 2(d), the SOC mixes spin and orbital angular momenta while preserving the total angular momentum, and $|P1_z^+, \uparrow(\downarrow)\rangle$ state is pushed down and the $|P2_z^-, \uparrow(\downarrow)\rangle$ state is pushed up, leading to the band inversion and parity exchange. In the nonmagnetic state, the important symmetries of the system are time-reversal symmetry Θ , inversion symmetry \mathcal{I} , three-fold rotation symmetry C_{3z} along the z axis and

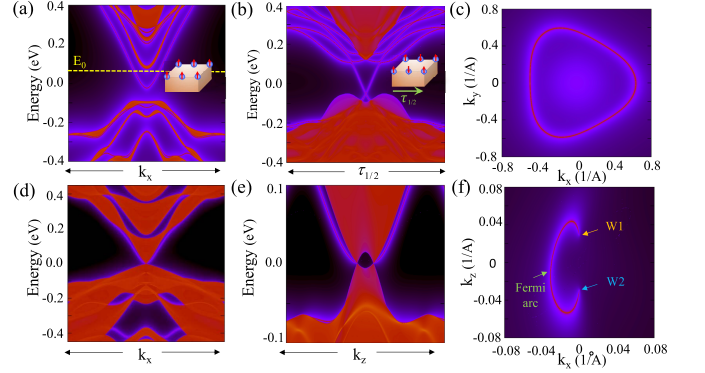


FIG. 4. Surface states. (a),(b), Energy and momentum dependence of the local density of states (LDOS) for AFM1 phase on the (111) and (011) surfaces, respectively. In (a), The surface states on (111) surface are fully gapped due to the \mathcal{S} symmetry broken. In (b), The gapless surface states can be seen at the Γ point with a linear dispersion in the bulk gap on the \mathcal{S} -preserving (011) surface. (c), Fermi surface on the (111) surface at the Energy level E_0 in (a) presents the triangle shape, different from the hexagonal shape in topological insulator Bi_2Se_3 . (d),(e), Energy and momentum dependence of the LDOS for FM1 phase on the (111) and (011) surfaces, respectively. In (e), the two Weyl points are seen along the k_z direction. (f), There are two Fermi arc connecting the Weyl points W1 and W2, indicating the ideal Weyl semimetal feature.

two-fold rotation symmetry C_{2x} along the x axis. In the basis of ($|P1_z^+, \uparrow\rangle, |P2_z^-, \uparrow\rangle, |P1_z^+, \downarrow\rangle, |P2_z^-, \downarrow\rangle$), the representation of the symmetry operations is given by $\Theta = 1_{2 \times 2} \otimes i\sigma^y \mathcal{K}$, $\mathcal{I} = \tau^z \otimes 1_{2 \times 2}$, $C_{3z} = \exp(i\pi/3 \sigma^z)$ and $C_{2x} = \exp(\tau^z \otimes i(\pi/2)\sigma^x)$, where \mathcal{K} is the complex conjugation operator, $\sigma^{x,y,z}$ and $\tau^{x,y,z}$ denote the Pauli matrices in the spin and orbital space, respectively. By requiring these four symmetries and keeping only the terms up to quadratic order in \mathbf{k} , we obtain the following generic form of the effective Hamiltonian for nonmagnetic state

$$\mathcal{H}_{\text{NM}}(\mathbf{k}) = \epsilon_0(\mathbf{k}) + \begin{pmatrix} M_\gamma(\mathbf{k}) & A_1 k_z & 0 & A_2 k_- \\ A_1 k_z & -M_\gamma(\mathbf{k}) & A_2 k_- & 0 \\ 0 & A_2 k_+ & M_\gamma(\mathbf{k}) & -A_1 k_z \\ A_2 k_+ & 0 & -A_1 k_z & -M_\gamma(\mathbf{k}) \end{pmatrix}, \quad (1)$$

where $k_\pm = k_x \pm ik_y$, $\epsilon_0(\mathbf{k}) = C + D_1 k_z^2 + D_2(k_x^2 + k_y^2)$ and $M_\gamma(\mathbf{k}) = M_0^\gamma + B_1^\gamma k_z^2 + B_2^\gamma(k_x^2 + k_y^2)$.

The FM1 state breaks Θ and C_{2x} but preserves the combined $C_{2x}\Theta$, therefore the effective Hamiltonian for FM1 is obtained by adding perturbative term $\delta\mathcal{H}_{\text{FM1}}(\mathbf{k})$ respecting the corresponding symmetries into $\mathcal{H}_{\text{NM}}(\mathbf{k})$, which is

$$\delta\mathcal{H}_{\text{FM1}}(\mathbf{k}) = \begin{pmatrix} M_1(\mathbf{k}) & A_3 k_z & 0 & A_4 k_- \\ A_3 k_z & M_2(\mathbf{k}) & -A_4 k_- & 0 \\ 0 & -A_4 k_+ & -M_1(\mathbf{k}) & A_3 k_z \\ A_4 k_+ & 0 & A_3 k_z & -M_2(\mathbf{k}) \end{pmatrix}, \quad (2)$$

where $M_{1,2}(\mathbf{k}) = M_\alpha(\mathbf{k}) \pm M_\beta(\mathbf{k})$, and $M_j(\mathbf{k}) = M_0^j + B_1^j k_z^2 + B_2^j (k_x^2 + k_y^2)$ with $j = \alpha, \beta$. By fitting the energy spectrum of the effective Hamiltonian with that of the first-principles calculation, the parameters in the effective model can be determined, which can be found in the Supplementary Material [48]. The $M_{1,2}$ terms characterize the Zeeman coupling with the magnetized Mn orbitals, and in general $M_1 \neq M_2$ denotes the different effective g -factor of $|P1_z^+, \uparrow(\downarrow)\rangle$ and $|P2_z^-, \uparrow(\downarrow)\rangle$.

The AFM1 state breaks Θ but preserves $\mathcal{S} = 1_{2 \times 2} \otimes i\sigma^y \mathcal{K} e^{i\mathbf{k} \cdot \boldsymbol{\tau}_{1/2}}$, and the unit cell doubles compared to FM1 state. One can construct the effective Hamiltonian for AFM1 from the model for FM1 state by considering two septuple layers with opposite magnetization, which will include eight bands. For simplicity, we obtain the four-band model similar to the above analysis. From band structure analysis, the four bands close the Fermi energy in the AFM1 state are the new bonding state $|P1_z^+, \uparrow(\downarrow)\rangle$ of four Bi layers and the antibonding state $|P2_z^-, \uparrow(\downarrow)\rangle$ of four Te layers (two Te1 and two Te4 in neighboring septuple layers). In the basis of ($|P1_z^+, \uparrow\rangle$, $|P2_z^-, \uparrow\rangle$, $|P1_z^+, \downarrow\rangle$, $|P2_z^-, \downarrow\rangle$), by requiring the symmetries \mathcal{I} , C_{3z} and \mathcal{S} , we get the effective Hamiltonian for AFM1 which has the same expression as $\mathcal{H}_{\text{NM}}(\mathbf{k})$ but with different parameters, namely

$$\mathcal{H}_{\text{AFM1}}(\mathbf{k}) = \epsilon'_0(\mathbf{k}) + \begin{pmatrix} M'(\mathbf{k}) & A'_1 k_z & 0 & A'_2 k_- \\ A'_1 k_z & -M'(\mathbf{k}) & A'_2 k_- & 0 \\ 0 & A'_2 k_+ & M'(\mathbf{k}) & -A'_1 k_z \\ A'_2 k_+ & 0 & -A'_1 k_z & -M'(\mathbf{k}) \end{pmatrix}, \quad (3)$$

where $\epsilon'_0(\mathbf{k}) = C' + D'_1 k_z^2 + D'_2 (k_x^2 + k_y^2)$ and $M'(\mathbf{k}) = M'_0 + B'_1 k_z^2 + B'_2 (k_x^2 + k_y^2)$. The fitting parameters are listed in the Supplementary Material [48]. We notice that $M'_0 < 0$ and $B'_1, B'_2 > 0$, which correctly characterizes the band inversion around $\mathbf{k} = 0$ and the topologically non-trivial nature of the system. The formation of the model in Eq. (3) is the same as that for topological insulator in Bi_2Se_3 [10].

Axion state and topological response. Such axion state has gapped bulk and surface states, and nonzero topological electromagnetic response described by the topological θ term, $S_\theta = (\theta/2\pi)(\alpha/2\pi) \int d^3x dt \mathbf{E} \cdot \mathbf{B}$. Here, \mathbf{E} and \mathbf{B} are the conventional electromagnetic fields inside the insulator, $\alpha = e^2/\hbar c$ is the fine-structure constant, e is the charge of an electron, and θ is the dimensionless pseudoscalar parameter describing the axion insulator. The axion state can be obtained by gapping all the \mathcal{S} -preserving surfaces from AFM1 MnBi_2Te_4 , which can be simply obtained by growing realistic materials without any \mathcal{S} -preserving surfaces or applying a small in plane magnetic field. Physically, θ has an explicit microscopic expression of the momentum space Chern-Simons form [34, 49]

$$\theta = \frac{1}{4\pi} \int d^3k \epsilon^{ijk} \text{Tr} \left[\mathcal{A}_i \partial_j \mathcal{A}_k + i \frac{2}{3} \mathcal{A}_i \mathcal{A}_j \mathcal{A}_k \right], \quad (4)$$

where $\partial_j = \partial/\partial k_j$, $\mathcal{A}_i^{\mu e}(\mathbf{k}) = -i \langle u_{\mathbf{k}}^\mu | \partial_i | u_{\mathbf{k}}^e \rangle$ is the momentum space non-abelian gauge field, with $|u_{\mathbf{k}}^\mu\rangle$ and $|u_{\mathbf{k}}^e\rangle$ referring to the periodic part of the Bloch function of the occupied bands. All physical quantities in the bulk depend on θ only modulo 2π . As θ is odd under time-reversal and parity operation, only time-reversal- and parity-breaking perturbations can induce a change of θ . The Mn sites always act as the inversion center, therefore, θ of the axion state is the same as that of AFM1 state, where $\theta = \pi$ is guaranteed by the \mathcal{S} symmetry. Such axion state emerged in MnBi_2Te_4 provides an ideal platform for quantized topological magnetoelectric effect [34, 50], which has not been experimentally observed, and is different from proposed axion state in the ferromagnet-topological insulator heterostructure where the gapless surface states on side surfaces are hard to eliminate [50–52]. Experimentally, such quantized topological magnetoelectric effect can be observed by measuring the induction of a parallel polarization current when an ac magnetic field is applied [50], which is $\mathcal{J} = (\theta/\pi)(e^2/2h)(\partial B_x/\partial t)\ell d$. Here, d and ℓ are the thickness and width of the MnBi_2Te_4 sample. For an estimation, taking $B_x = B_0 e^{-i\omega t}$, $B_0 = 10$ G, $\omega/2\pi = 1$ GHz, $d = 50$ nm, $\theta = \pi$, and $\ell = 400$ μm , we have $\mathcal{J} = -i\mathcal{J}_0 e^{-i\omega t}$ with $\mathcal{J}_0 = 2.22$ nA, in the range accessible by experiments.

It is worth mentioning that the Néel order in AFM1 state is essentially different from the Néel order in the dynamical axion field proposed in Ref. [40]. In the latter case, the Néel order breaks the time-reversal symmetry Θ and parity \mathcal{I} , but conserves $\mathcal{I}\Theta$. The magnetic fluctuation of the Néel order leads to linear contribution to the fluctuation of axion field, and the static θ deviates from π . While in the case of AFM1 MnBi_2Te_4 , the Néel order conserves both \mathcal{I} and \mathcal{S} , thus the static $\theta = \pi$, and to the linear order, the magnetic fluctuation has no contribution to the dynamics of axion field.

Materials. Other tetradymite-type compounds XBi_2Te_4 , XBi_2Se_4 and XSb_2Te_4 ($X = \text{Mn}$ or Eu), if with the same rhombohedral crystal structure, are also promising candidates to host magnetic topological states similar to MnBi_2Te_4 . Actually, tetradymite-type compounds $\text{XB} \cdot \text{A}_2\text{B}_3$ belong to a large class of ternary chalcogenides materials $(\text{XB})_n \cdot (\text{A}_2\text{B}_3)_m$ with $X = (\text{Ge}, \text{Sn}$ or $\text{Pb})$, $A = (\text{Sb}$ or $\text{Bi})$ and $B = (\text{Se}$ or $\text{Te})$, most of which were found to be topological insulators [53]. Interestingly, $(\text{GeTe})_n (\text{Sb}_2\text{Te}_3)_m$ and $(\text{GeTe})_n (\text{Bi}_2\text{Te}_3)_m$ have been widely studied as phase change memory materials [54]. By tuning the layer index m and n , we can play with the crystal structure, the topological property, and the magnetic property of the series of materials $(\text{XB})_n \cdot (\text{A}_2\text{B}_3)_m$, which opens a broad way to study emergent phenomena of magnetic topological states.

We thank Ke He for stimulating discussions. This work is supported by the Natural Science Foundation of China (Grant No. 11674165, 11774065, 11834006),

the Fok Ying-Tong Education Foundation of China (Grant No. 161006), the National Key Research Program of China under Grant No. 2016YFA0300703, the Natural Science Foundation of Shanghai (Grant No. 17ZR1442500), the Open Research Fund Program of the State Key Laboratory of Low-Dimensional Quantum Physics (Contract No. KF201606), and by Fudan University Initiative Scientific Research Program.

Note added: Recently, we learned of the experimental papers in the same material by Gong *et al* [55] and Otrokov *et al* [56].

* zhanghj@nju.edu.cn

† wjingphys@fudan.edu.cn

- [1] M. Z. Hasan and C. L. Kane, *Rev. Mod. Phys.* **82**, 3045 (2010).
- [2] X.-L. Qi and S.-C. Zhang, *Rev. Mod. Phys.* **83**, 1057 (2011).
- [3] C.-K. Chiu, J. C. Y. Teo, A. P. Schnyder, and S. Ryu, *Rev. Mod. Phys.* **88**, 035005 (2016).
- [4] N. P. Armitage, E. J. Mele, and A. Vishwanath, *Rev. Mod. Phys.* **90**, 015001 (2018).
- [5] C. L. Kane and E. J. Mele, *Phys. Rev. Lett.* **95**, 226801 (2005).
- [6] B. A. Bernevig, T. L. Hughes, and S.-C. Zhang, *Science* **314**, 1757 (2006).
- [7] M. König, S. Wiedmann, C. Brüne, A. Roth, H. Buhmann, L. Molenkamp, X.-L. Qi, and S.-C. Zhang, *Science* **318**, 766 (2007).
- [8] X. Qian, J. Liu, L. Fu, and J. Li, *Science* **346**, 1344 (2014).
- [9] Y. Xia, D. Qian, D. Hsieh, L. Wray, A. Pal, H. Lin, A. Bansil, D. Grauer, Y. S. Hor, R. J. Cava, and M. Z. Hasan, *Nature Phys.* **5**, 398 (2009).
- [10] H. Zhang, C.-X. Liu, X.-L. Qi, X. Dai, Z. Fang, and S.-C. Zhang, *Nature Phys.* **5**, 438 (2009).
- [11] Y. L. Chen, J. G. Analytis, J. H. Chu, Z. K. Liu, S. K. Mo, X. L. Qi, H. J. Zhang, D. H. Lu, X. Dai, Z. Fang, S. C. Zhang, I. R. Fisher, Z. Hussain, and Z. X. Shen, *Science* **325**, 178 (2009).
- [12] H. Weng, C. Fang, Z. Fang, B. A. Bernevig, and X. Dai, *Phys. Rev. X* **5**, 011029 (2015).
- [13] S.-M. Huang, S.-Y. Xu, I. Belopolski, C.-C. Lee, G. Chang, B. Wang, N. Alidoust, G. Bian, M. Neupane, C. Zhang, S. Jia, A. Bansil, H. Lin, and M. Z. Hasan, *Nature Commun.* **6**, 7373 (2015).
- [14] A. A. Soluyanov, D. Gresch, Z. Wang, Q. Wu, M. Troyer, X. Dai, and B. A. Bernevig, *Nature* **527**, 495 (2015).
- [15] S.-Y. Xu, I. Belopolski, N. Alidoust, M. Neupane, G. Bian, C. Zhang, R. Sankar, G. Chang, Z. Yuan, C.-C. Lee, S.-M. Huang, H. Zheng, J. Ma, D. S. Sanchez, B. Wang, A. Bansil, F. Chou, P. P. Shibayev, H. Lin, S. Jia, and M. Z. Hasan, *Science* **349**, 613 (2015).
- [16] B. Q. Lv, H. M. Weng, B. B. Fu, X. P. Wang, H. Miao, J. Ma, P. Richard, X. C. Huang, L. X. Zhao, G. F. Chen, Z. Fang, X. Dai, T. Qian, and H. Ding, *Phys. Rev. X* **5**, 031013 (2015).
- [17] F.-f. Zhu, W.-j. Chen, Y. Xu, C.-l. Gao, D.-d. Guan, C.-h. Liu, D. Qian, S.-C. Zhang, and J.-f. Jia, *Nature Mat.* **14**, 1020 (2015).
- [18] L. Lu, J. D. Joannopoulos, and M. Soljačić, *Nature Photon.* **8**, 821 (2014).
- [19] J. Ruan, S.-K. Jian, H. Yao, H. Zhang, S.-C. Zhang, and D. Xing, *Nat. Commun.* **7**, 11136 (2016).
- [20] B. Bradlyn, J. Cano, Z. Wang, M. G. Vergniory, C. Felser, R. J. Cava, and B. A. Bernevig, *Science* **353**, aaf5037 (2016).
- [21] Z. Wang, A. Alexandradinata, R. J. Cava, and B. A. Bernevig, *Nature* **532**, 189 (2016).
- [22] B. Lv, Z.-L. Feng, Q.-N. Xu, X. Gao, J.-Z. Ma, L.-Y. Kong, P. Richard, Y.-B. Huang, V. Strocov, C. Fang, *et al.*, *Nature* **546**, 627 (2017).
- [23] H. Zhou, C. Peng, Y. Yoon, C. W. Hsu, K. A. Nelson, L. Fu, J. D. Joannopoulos, M. Soljačić, and B. Zhen, *Science* **359**, 1009 (2018).
- [24] S. Wu, V. Fatemi, Q. D. Gibson, K. Watanabe, T. Taniguchi, R. J. Cava, and P. Jarillo-Herrero, *Science* **359**, 76 (2018).
- [25] T. Zhang, Y. Jiang, Z. Song, H. Huang, Y. He, Z. Fang, H. Weng, and C. Fang, *ArXiv e-prints*: , 1807.08756 (2018).
- [26] F. Tang, H. C. Po, A. Vishwanath, and X. Wan, *ArXiv e-prints*: , 1807.09744 (2018).
- [27] M. G. Vergniory, L. Elcoro, C. Felser, B. A. Bernevig, and Z. Wang, *ArXiv e-prints*: , 1807.10271 (2018).
- [28] C.-Z. Chang, J. Zhang, X. Feng, J. Shen, Z. Zhang, M. Guo, K. Li, Y. Ou, P. Wei, L.-L. Wang, Z.-Q. Ji, Y. Feng, S. Ji, X. Chen, J. Jia, X. Dai, Z. Fang, S.-C. Zhang, K. He, Y. Wang, L. Lu, X.-C. Ma, and Q.-K. Xue, *Science* **340**, 167 (2013).
- [29] R. S. K. Mong, A. M. Essin, and J. E. Moore, *Phys. Rev. B* **81**, 245209 (2010).
- [30] X. Wan, A. M. Turner, A. Vishwanath, and S. Y. Savrasov, *Phys. Rev. B* **83**, 205101 (2011).
- [31] G. Xu, H. Weng, Z. Wang, X. Dai, and Z. Fang, *Phys. Rev. Lett.* **107**, 186806 (2011).
- [32] P. Tang, Q. Zhou, G. Xu, and S.-C. Zhang, *Nature Phys.* **12**, 1100 (2016).
- [33] G. Hua, S. Nie, Z. Song, R. Yu, G. Xu, and K. Yao, *ArXiv e-prints*: , 1801.02806 (2018).
- [34] X.-L. Qi, T. L. Hughes, and S.-C. Zhang, *Phys. Rev. B* **78**, 195424 (2008).
- [35] L. Wu, M. Salehi, N. Koirala, J. Moon, S. Oh, and N. P. Armitage, *Science* **354**, 1124 (2016).
- [36] J. Wang and S.-C. Zhang, *Nature Mat.* **16**, 1062 (2017).
- [37] R. Yu, W. Zhang, H.-J. Zhang, S.-C. Zhang, X. Dai, and Z. Fang, *Science* **329**, 61 (2010).
- [38] J. Wang, B. Lian, and S.-C. Zhang, *Phys. Scr.* **2015**, 014003 (2015).
- [39] L. Šmejkal, Y. Mokrousov, B. Yan, and A. H. MacDonald, *Nature Phys.* **14**, 242 (2018).
- [40] R. Li, J. Wang, X. L. Qi, and S. C. Zhang, *Nature Phys.* **6**, 284 (2010).
- [41] L. Šmejkal, J. Železný, J. Sinova, and T. Jungwirth, *Phys. Rev. Lett.* **118**, 106402 (2017).
- [42] J. Wang, *ArXiv e-prints*: , 1701.00896 (2017).
- [43] H. Zhang, J. Wang, G. Xu, Y. Xu, and S.-C. Zhang, *Phys. Rev. Lett.* **112**, 096804 (2014).
- [44] D. S. Lee, T.-H. Kim, C.-H. Park, C.-Y. Chung, Y. S. Lim, W.-S. Seo, and H.-H. Park, *CrystEngComm* **15**, 5532 (2013).
- [45] M. M. Otrokov, T. V. Menshchikova, M. G. Vergniory, I. P. Rusinov, A. Y. Vyazovskaya, Y. M. Koroteev,

- G. Bihlmayer, A. Ernst, P. M. Echenique, A. Arnau, and E. V. Chulkov, *2D Mater.* **4**, 025082 (2017).
- [46] L. Fu and C. L. Kane, *Phys. Rev. B* **76**, 045302 (2007).
- [47] R. Yu, X. L. Qi, A. Bernevig, Z. Fang, and X. Dai, *Phys. Rev. B* **84**, 075119 (2011).
- [48] See Supplemental Material for technical details.
- [49] A. M. Essin, J. E. Moore, and D. Vanderbilt, *Phys. Rev. Lett.* **102**, 146805 (2009).
- [50] J. Wang, B. Lian, X.-L. Qi, and S.-C. Zhang, *Phys. Rev. B* **92**, 081107 (2015).
- [51] M. Mogi, M. Kawamura, R. Yoshimi, A. Tsukazaki, Y. Kozuka, N. Shirakawa, K. S. Takahashi, M. Kawasaki, and Y. Tokura, *Nature Mater.* **16**, 516 (2017).
- [52] D. Xiao, J. Jiang, J.-H. Shin, W. Wang, F. Wang, Y.-F. Zhao, C. Liu, W. Wu, M. H. W. Chan, N. Samarth, and C.-Z. Chang, *Phys. Rev. Lett.* **120**, 056801 (2018).
- [53] H. Jin, J.-H. Song, A. J. Freeman, and M. G. Kanatzidis, *Phys. Rev. B* **83**, 041202 (2011).
- [54] M. Wuttig and N. Yamada, *Nature Mater.* **6**, 824 (2007).
- [55] Y. Gong *et al.*, arXiv: 1809.07926 (2018).
- [56] M. M. Otrokov *et al.*, arXiv: 1809.07389 (2018).